Smart bodysuit integrating digital twin technology for real-time human motion monitoring and visualization

Peng Jin, Runtian Jiang, Rong Zheng, Qing Chen, Jintu Fan

***Abstract*—Real-time motion monitoring can have many significant applications in fields such as smart healthcare, human-computer interaction, sports training and fashion metaverse. However, current wearable systems used for motion monitoring suffer from issues related to usability, comfort, interactivity, and accuracy. To address these challenges, this work proposes a smart bodysuit system that integrates digital twin technology for real-time human motion monitoring and visualization. The system comprises novel hardware and software including a specially designed knitted bodysuit housing the electronic components to reduce calibration errors, a data calibration method to take into account the possible clothing-skeleton misalignment, an adaptive-threshold method combining random forest and zero-speed update algorithms to enhance motion recognition accuracy, and an enhanced TCP-Illinois congestion control algorithm to reduce system latency. Furthermore, digital twin technology is incorporated to improve human-computer interaction. Wearer trial tests showed that the system exhibits low latency, high accuracy, and good comfort and wearability. The network latency test showed a delay of 13.17 milliseconds, which is comparable to or even better than commercial systems. The testing error of the joint angle can be controlled within 0.2°, and the recognition accuracy of the motion pattern can reach 98.6%. The proposed adaptive-threshold method has higher positioning accuracy compared to the existing fixed-threshold method. Furthermore, the smart bodysuit system can reconstruct real-time wearer's motion states through digital twin technology. The developed system is believed to have potential significant applications in the metaverse, digital healthcare, home monitoring, and sports science.**

Index Terms — **Smart bodysuit, motion monitoring, digital twin, Internet of Things, inertial sensor**

I. INTRODUCTION

EFFECTIVELY monitoring human motion parameters holds many significant applications such as including health assessment [1], smart healthcare [2], human-computer interaction [3], virtual reality [4], film production [5], video games [6], and industrial robotics [7]. This monitoring covers specific activities such as motion posture tracking, long-term correction and optimization of incorrect postures in daily scenarios, and the diagnosis and observation of particular patient groups [8]. By analyzing human motion data, a deeper understanding of an individual's physical condition, motor abilities, and behavioral habits can be achieved, enabling the implementation of targeted preventive, intervention, and improvement measures [9]. These technologies, through precise motion capture and recognition, not only enhance the interactive experience and efficiency across various applications but also promote personalized services and intelligent advancements in fields such as healthcare, sports, and entertainment [10].

With the constant development of the Internet of Things (IoT) and Artificial Intelligence, motion recognition or capture devices have grown considerably [11], [12], [13]. Currently, common motion capture devices include optical-based systems and inertial-based systems [14], [15]. Optical-based motion capture systems primarily utilize computer vision principles [16], offering advantages such as high accuracy, suitability for capturing complex movements, tracking motion trajectories of multiple joints, and enabling real-time motion analysis [17], [18], [19], [20].

Compared to optical-based motion capture devices, inertial-based motion capture devices offer significant advantages, including small size, low cost, and high robustness in different environments [21], [22], [23]. Inertial-based motion capture refers to the integration of motion sensors (IMUs) into small modules attached to different parts of the body, with the human motion recorded by these sensors and later analyzed algorithmically to generate motion data [24], [25], [26]. Currently, many commercial inertial motion capture devices, such as Xsens [27] and Notiom [28], are available. However, these products typically use strap-based sensor attachment methods in most application scenarios. Additionally, the motion capture suits provided by these

This work was supported by the Fundamental Research Funds for the Central Universities and Graduate Student Innovation Fund of Donghua University [Grant Number: CUSF-DH-D-2024021]; the China Scholarship Council program [Grant Number: 202406630006]; Natural Science Foundation of Shanghai: [Grant Number 21ZR1400100]; Arts and Humanities Research Council: [Grant Number AH/T011483/1]; Shanghai Style Fashion Design & Value Creation Collaborative Innovation Center: [Grant Number ZX201311000031]. (Corresponding author: Rong Zheng and Jintu Fan)

Peng Jin is with College of Fashion and Design, Donghua University, Shanghai 200051, China, and also with College of Design and Engineering, National University of Singapore, Singapore 117575, Singapore (e-mail: 925212692@qq.com).

Runtian Jiang is with College of Fashion and Design, Donghua University, Shanghai 200051, China (e-mail: pamonaj@foxmail.com).

Rong Zheng and Qing Chen are with Shanghai International Fashion Innovation Centre, Donghua University, Shanghai 200051, China (e-mail: rzheng@dhu.edu.cn; chenqing@dhu.edu.cn).

Jintu Fan is with Institute of Textiles and Clothing, The Hong Kong Polytechnic University, Kowloon, Hong Kong, China, and also with Shanghai International Fashion Innovation Centre, Donghua University, Shanghai 200051, China (e-mail: jin-tu.fan@polyu.edu.hk).

brands often utilize heavy, non-elastic fabrics and plastic slots to secure the sensors, preventing slippage between the clothing and sensors that could lead to inaccurate data collection.

In conclusion, despite the increasing application of inertial-based motion capture devices in human motion monitoring, several technical challenges and unresolved issues persist, such as poor comfort and accuracy of the devices for prolonged wear, poor wearability of strap-on carriers, poor usability of products, and unclear methods for human-computer interaction, failing to meet the demand for comprehensive, accurate, and comfortable monitoring of human motion data.

In recent years, the rapid advancement of smart textiles [29], [30] and digital twin (DT) technology [31] offers promising solutions to the aforementioned limitations. Smart clothing—clothing integrated with sensing, actuation, or data transmission capabilities—enable continuous, body-conformable motion tracking while maintaining high wearability and user comfort [32]. Compared to conventional wearable systems, smart clothing can utilize lightweight, flexible materials and embedded electronics to minimize discomfort and improve long-term usability [33].

In parallel, digital twin technology has gained traction as a novel paradigm in biomedical applications, enabling dynamic, real-time mapping of the physical body into a virtual replica for enhanced visualization, interaction, and feedback [34]. While digital twins were initially developed in the manufacturing and industrial sectors, their application is rapidly expanding into healthcare, rehabilitation, and the metaverse. In the context of human motion monitoring, digital twins offer new capabilities such as intuitive visual feedback, remote diagnosis, and bi-directional human–machine interaction by synchronizing physical motion data with high-fidelity virtual models in real time [31].

To this end, we propose a smart bodysuit system that synergistically combines smart clothing with digital twin modeling to enable real-time, precise, and user-friendly motion monitoring. This integration aims to address existing shortcomings in wearability, data fidelity, and human–computer interaction across diverse application domains.

The main contributions of this work are summarized as follows:

1) A data calibration method that considers the misalignment between clothing and the human body was proposed, eliminating the need for straps or heavy tight-fitting garments when collecting motion data, thereby enhancing the comfort, wearability, and accuracy of motion data collection.

2) An adaptive thresholding method, which combines the Random Forest (RF) algorithm and Zero-Update of Velocity (ZUPT) algorithm, was proposed and validated to further improve the accuracy of motion recognition.

3) Based on inertial sensors and IoT technology, a comfortable, user-friendly, and high-precision smart body suit system for human motion data monitoring and 3D virtual mapping was proposed, and the digital twin technology was integrated into the intelligent bodysuit system to achieve data synchronization between digital space and real space, providing a new way of human-computer interaction.

The structure of this work is as follows: Section 2 introduces the system architecture and components. Section 3 describes the method for developing the smart bodysuit system. Section 4 presents the experimental results and the potential application prospects of the smart body suit system in human-computer interaction. The conclusion is provided in Section 5.

II. System Composition

Based on the IoT architecture, the smart onesie system is divided into two main components: the physical system and the virtual system. The physical system comprises the clothing and hardware modules used for collecting and transmitting human motion data, the virtual system includes 3D modeling software and digital twin models used for receiving and displaying motion data. As shown in Figure 1.

A. Physical system

The physical system mainly consists of three parts: clothing, electronic modules, and computer or mobile phone.

1) Clothing: A highly flexible long-sleeved knit bodysuit was designed to carry the electronic module, with its unique softness and close-fitting nature, allows for the accurate collection of human motion data while ensuring comfort.

2) Electronic modules: Including sensors, controller modules, power modules, used for collecting motion data. Motion data was collected in a non-contact manner, and efforts were made to optimize the size of the hardware to ensure the comfort of wearing the clothing system. Additionally, all non-washable hardware modules were designed to be detachable to ensure the washability of the clothing.

3) Computer or mobile phone: Used to establish a wireless connection with the hardware modules and receive motion data collected by sensors.

B. Virtual System

The virtual system consists of the host software and digital twin models running on the computer or mobile phone, which was primarily used to map the physical model of the smart bodysuit and the real environment into the 3D software, and the virtual model of the motion state and the actual environment was displayed to provide a more intuitive and convenient human-computer interaction experience.

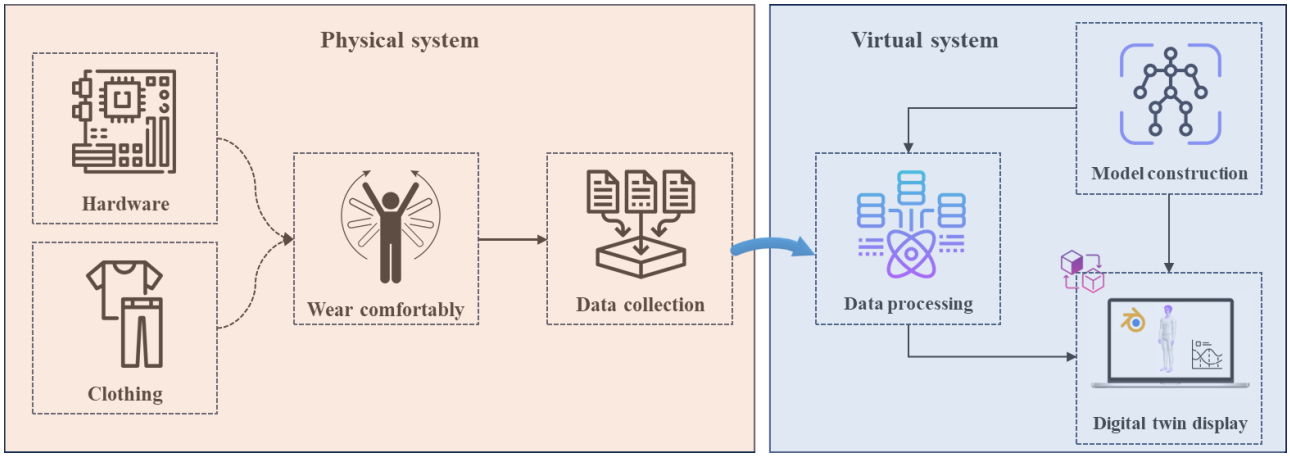

Fig.1 System composition and overall process.

III. METHOD

A. Design and development methods for clothing

In terms of comfort during prolonged wear, clothing far surpasses traditional wearable devices. Clothing for this purpose must be soft, skin-friendly, and comfortable to wear, while also ensuring accurate motion data collection through a good fit and sufficient extensibility. Therefore, knitted bodysuit was chosen as the clothing carrier in the smart bodysuit system proposed in this work. The unique elasticity and fit of knitted bodysuit effectively reduce data errors caused by sensor loosening during human movement [35]. To ensure the aesthetics of the clothing, seamless integration areas were established on the torso and limbs of the clothing to create invisible pockets for accommodating hardware modules. The seamless integration areas consist of a fabric layer and a Polyurethane Reactive (PUR) hot-melt adhesive layer applied to the fabric layer. The fabric layer and PUR layer were thermally pressed together to form seamless fitting areas, and the color of the pocket fabric matches that of the clothing fabric.

B. Human kinematics modelling and sensor location

The kinematic model of the human body can be simplified as a multi-link model, by constructing this multi-link model, expressions for the interaction torques at various joints of the human body can be directly obtained, facilitating dynamic coupling and coordination analysis of multi-joint movements. The structure of the clothing is similar as the multi-link model, as it can be divided into a tree-like structure composed of multiple rigid segments. Therefore, clothing design exhibits unique advantages in the research field of multi-joint motion control [36],[37]. From an ergonomic perspective, areas with fewer muscles, such as the left and right back shoulders, the back, the sides of the left and right arms, the coccyx point at the back, and the sides of the left and right legs, show less impact on the sensors [38], [39]. Therefore, invisible pockets for carrying hardware devices were positioned in these areas.

Taking the right hand B_1 as an example, it typically rotates only around the x_1 axis of its own coordinate system, corresponding to the anatomical concepts of flexion and extension. Let the length of the forearm be L_1. Then, by rotating the right hand coordinate system around the y_{b1} axis by $-q_1$ degrees and translating along the x_{b1} axis by L_1, we can transform to the forearm coordinate system. The coordinate transformation matrix A_1 is given by:

$$A_1 = Rot(x,-q_1) \times Trans(0,0,-L_1) = \begin{bmatrix} 1 & 0 & 0 & 0 \\ 0 & \cos q_1 & \sin q_1 & -L_1 \cdot \sin q_1 \\ 0 & -\sin q_1 & \cos q_1 & -L_1 \cdot \cos q_1 \\ 0 & 0 & 0 & 1 \end{bmatrix} \quad (1)$$

Similarly, let the length of the upper arm be L_2. The transformation to the upper arm coordinate system can be achieved by translating the forearm coordinate system along the x_{b2} axis by $-L_2$, rotating around the y_{b2} axis by q_1 degrees, and around the z_{b2} axis by $-q_1$ degrees. The transformation matrix A_2 is computed as follows:

$$A_2 = Rot(y,q_1) \times Rot(z,-q_2) \times Trans(0,0,-L_2) = \begin{bmatrix} \cos q_1 \cdot \cos q_2 & \cos q_1 \cdot \sin q_2 & \sin q_1 & -L_2 \cdot \sin q_1 \\ -\sin q_1 & \cos q_2 & 0 & 0 \\ -\sin q_1 \cdot \cos q_2 & -\sin q_1 \cdot \sin q_2 & \cos q_1 & -L_2 \cdot \cos q_1 \\ 0 & 0 & 0 & 1 \end{bmatrix} \quad (2)$$

Consequently, we can sequentially calculate the pose equations A_3 for the upper arm relative to the three sensors on the upper torso, and A_4 for the upper torso relative to the lower torso. The positional relationships between points within the upper and lower torso can also be determined based on the aforementioned principles, as illustrated in Figure 2.

$$A_3 = \begin{bmatrix} -C_2C_3 & C_2S_3 & S_2 & D_1C_2S_3 \\ -S_1S_2S_3 + C_1S_3 & S_1S_2S_3 + C_1C_3 & -S_1C_2 & D_1S_1C_2 \\ -C_1S_2C_3 - S_1S_3 & C_1S_2S_3 - S_1C_3 & -C_1C_2 & D_2C_1C_2 \\ 0 & 0 & 0 & 1 \end{bmatrix} \quad (3)$$

$$A_4 = \begin{bmatrix} C_2C_3 & C_2S_3 & -S_2 & D_1 \cdot S_2 \\ S_1S_2C_3 - C_1S_3 & S_1S_2S_3 + C_1C_3 & S_1C_2 & -D_1 \cdot S_1C_2 \\ C_1S_2C_3 + S_1S_3 & C_1S_2S_3 - S_1C_3 & C_1C_2 & -D_1 \cdot C_1C_2 \\ 0 & 0 & 0 & 1 \end{bmatrix} \quad (4)$$

where D_1 and D_2 denote the position of the shoulder joint relative to the thoracic joint, S_i and C denote $sinq_i$ and $cosq_i$, respectively (i=1,2,3).

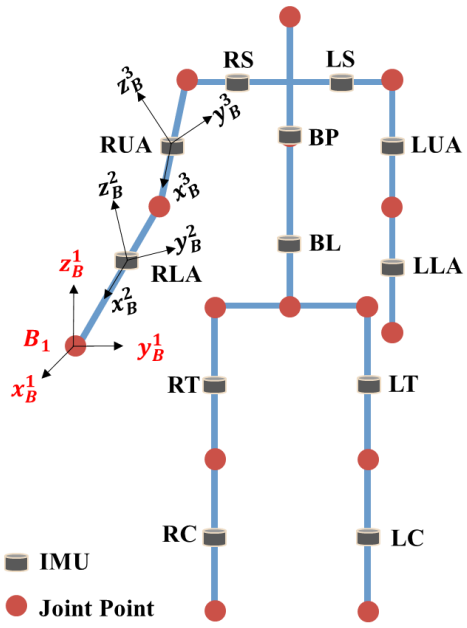

Fig.2 Kinematic model of the human body.

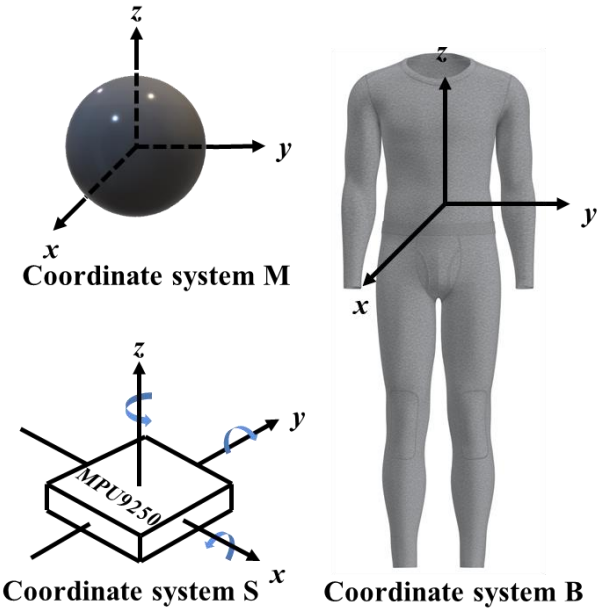

Fig.3 Definition of the coordinate system.

C. Design and development method of hardware modules

Unlike traditional wearable carriers, which have less requirements for the size, weight, and integration of hardware modules, using flexible knitted bodysuit as a carrier imposes higher demands. Too high weights and large dimensions of hardware modules can adversely affect data collection. Therefore, in this work, a small hardware module was developed according to the requirements.

The module consists of an IMU (MPU9250, TDK InvenSense, USA), a main control unit (ESP32, Loxin Technology, China), and a power supply (3.7V lithium battery, Telesky, China). Altium Designer was used for the module design, and lightweight epoxy resin was used for the module substrate. The modules were encapsulated using 3D printing technology, and the weight of the encapsulated individual module was about 10g. It was verified that this weight did not damage the integrity of the clothing fabric.

D. Methods for calibrating positioning errors

Compared to using straps or plastic bases to secure sensors, utilizing soft clothing and pockets to carry sensors demands higher accuracy requirements for the sensors. This is because flexible clothing tends to misalign with the sensors during movement. To address this issue, this study proposes a method for correcting positioning errors.

1) **Definition of coordinate system**

In this work, the global coordinate system was denoted as the M system, the sensor node coordinate system was denoted as the S system, and the clothing/human body coordinate system was denoted as the B system. As shown in Figure 3.

2) **Sensor error calibration**

IMUs can be susceptible to measurement errors arising from factors like the fabrication process and environmental conditions, necessitating the need to compensate for sensor errors beforehand. In this work, the accelerometer was calibrated by the six-face method, and the resting time of each face of the module was set to 5 minutes. Also, the module was left at rest for 30 min to get a good estimate of the gyroscope drift, while the magnetometer was calibrated using the ellipsoid fitting method [40].

3) **Calibration of positioning error**

Given that IMUs placed on clothing may encounter discrepancies in skeletal positioning, as shown in Figure 4, it is necessary to calibrate this error in advance.

The initial posture of the human body was set as T-pose, which is a standardized posture that provides a uniform reference point, ensuring that each motion capture session begins from an identical stance, thereby simplifying subsequent data processing and analysis. Assuming that the position of the IMU and the human skeleton was in an ideal state, the equation for calculating the joint angles of the human body is shown in Equation (5). After the error quaternion G_k^e was calculated, the joint angle of the body at the next moment (moment t) was calculated as shown in Equation (6). Since skeletal motion is always driven by one bone to the next bone, the equation for calculating the joint angle between two bones can be determined by Equation (3) when k-bone motion drives k-1-bone motion.

$$G_k^s \otimes q G_k^e = [1 \quad O_{1\times 3}] \tag{5}$$

$$G_k^j = G_k^t \otimes G_k^e \tag{6}$$

$$G_m^j = G \otimes G_{k-1}^j \tag{7}$$

Where: G_k^s is the static attitude quaternion of the sensor attached to the k skeleton of the human body, G_k^e is the error quaternion, G_k^t is the attitude quaternion of the sensor attached to the k skeleton solved by the attitude update at time t, G_k^j is

the joint angle quaternion between the k and the $k-1$ skeleton at time t, and G_{k-1}^{j} is the joint angle quaternion between the k and the $k-1$ skeleton at time t, G_{m}^{j} is the number of joint angle quaternions between k skeleton and $k-1$ skeleton at time t when $k-1$ skeleton is also in motion.

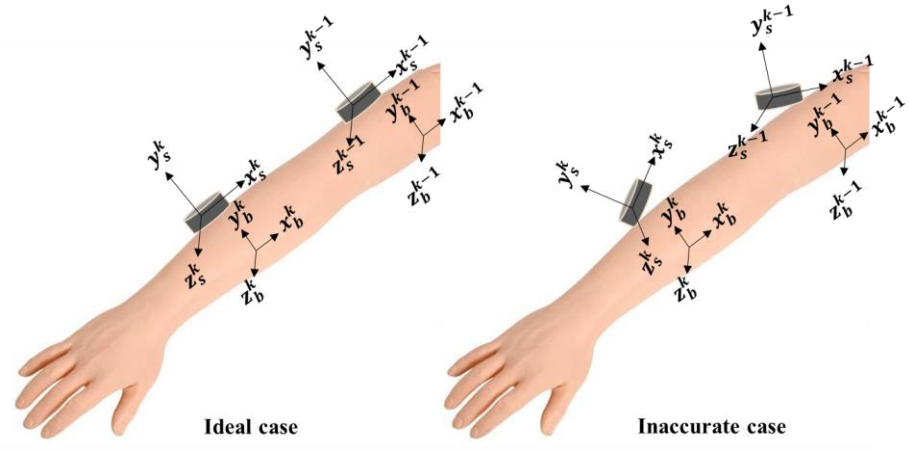

Fig. 3 Schematic representation of the error in clothing and skeleton.

E. Zero speed determination

IMU-based positioning mechanism essentially belongs to the waypoint projection positioning, where positioning errors from previous results will accumulate into current results. Additionally, due to the zero-bias of the IMU, the positioning errors will accumulate over time. To address this issue, an adaptive zero-speed detection mechanism based on RF algorithm for multi-motion modes is proposed.

1) State determination

During walking, the movement of the human foot follows a periodic pattern. There is a relatively stationary interval between two adjacent motion states when the foot contacts the ground, known as the zero-velocity interval, as shown in Figure 5. Accurately detecting the zero-velocity interval and performing error correction during this interval can effectively suppress error accumulation. In this work, a method based on joint determination using acceleration and angular velocity information was employed to determine the zero-velocity state. The zero-velocity determination at time t is expressed by Equations (8) and (9). Typically, at time t, if the acceleration and angular velocity information satisfies Equation (8), the state at that time is determined as zero velocity.

$$T(t) = \frac{1}{W}\sum_{i=t}^{t+W-1}\left(\frac{1}{\sigma_w^2}\|w(l)\|^2 + \frac{1}{\sigma_a^2}\left\|a(l) - g\frac{m_a}{\|m_a\|}\right\|^2\right) < \tau \tag{8}$$

$$m_a = \frac{1}{W}\sum_{i=t}^{t+W-1} a(l) \tag{9}$$

Where: $T(t)$ represents the function of acceleration and angular velocity at time t, w is the width of the time window, σ_w^2 is the standard deviation of angular velocity measurement error, σ_a^2 is the standard deviation of acceleration measurement error, g is the gravitational acceleration, $w(l)$ and $a(l)$ represent the angular velocity and acceleration values within the time window, respectively, $\|*\|$ denotes the 2-norm, ma represents the average acceleration of all samples within the time window, and τ denotes the threshold.

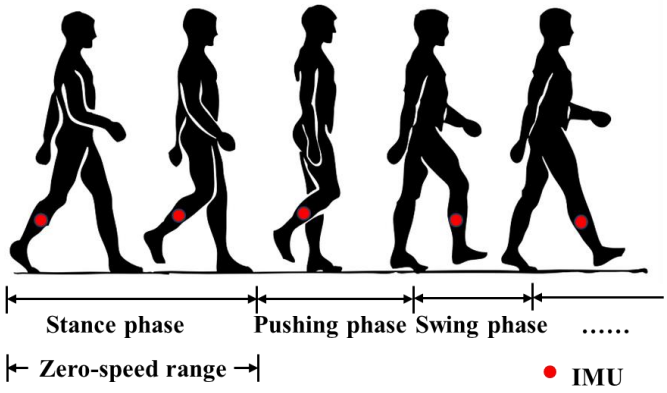

Fig. 5 Interval of human walking state.

2) Adaptive threshold setting

The proper selection of the zero-velocity detection threshold is crucial for accurately determining the zero-velocity state. In this work, an adaptive-threshold method that combines RF algorithm and ZUPT algorithm was proposed.

An IMU placed at the calf of the clothing was used to collect data information at a sampling frequency of 60Hz during five types of movements: standing, walking, running, ascending stairs, and descending stairs, the raw data of acceleration and angular velocity were obtained. Additionally, model training was conducted using the DIP-IMU dataset [41] and the TotalCapture dataset [42].

Feature extraction was conducted on the data, the feature vector can be represented as:

$$T = f(A) = (\mu, \sigma, m_{max}, m_{min}, S_k, r_{xy}, r_{xz}, r_{yz}, Q) \tag{10}$$

$$\mu = \frac{m_1+m_2+\cdots+m_n}{n} \tag{11}$$

$$\sigma = \sqrt{\frac{1}{n}\sum_{i=1}^{n}(s_i-\mu)^2} \tag{12}$$

$$S_k = \frac{n\sum_{i=1}^{n}(s_i-\mu)^3}{(n-1)(n-2)\sigma^3} \tag{13}$$

$$r_{xy} = \frac{\sum_{i=1}^{n}((x_i-\mu_x)(y_i-\mu_y))}{\sqrt{\sum_{i=1}^{n}(x_i-u_x)^2}\sqrt{\sum_{i=1}^{n}(y_i-u_y)^2}} \tag{14}$$

$$r_{yz} = \frac{\sum_{i=1}^{n}((y_i-\mu_y)(z_i-\mu_z))}{\sqrt{\sum_{i=1}^{n}(y_i-u_y)^2}\sqrt{\sum_{i=1}^{n}(z_i-u_z)^2}} \tag{15}$$

$$r_{xz} = \frac{\sum_{i=1}^{n}((x_i-\mu_x)(z_i-\mu_z))}{\sqrt{\sum_{i=1}^{n}(x_i-u_x)^2}\sqrt{\sum_{i=1}^{n}(z_i-u_z)^2}} \tag{16}$$

$$Q = Q_3 - Q_1 \tag{17}$$

Where: T is the feature vector, $f(A)$ is the arithmetic mean of sample A, μ is the arithmetic mean of samples, σ is the sample standard deviation; m_{max} is the maximum value of the samples, m_{min} is the minimum value of the samples, S_k is the skewness of the samples; r_{xy} represents the correlation coefficient between the x-axis and y-axis of the samples, Q is the interquartile range of the sample, x_i, y_i, z_i represent the data along the x, y, z axes respectively, u_x, u_y, u_z represent the arithmetic mean of the data along the x, y, z axes respectively.

The RF algorithm was utilized to classify and recognize the feature vectors of the five motion modes, with the decision tree counts set at 90. The feature vectors extracted from offline collected data were used as the training set to train the model, the feature vectors extracted from online collected data serve as the test set, and the recognition results can be obtained.

Following the determination of zero-speed thresholds and recognition results for the five motion patterns, a fusion approach was adopted wherein the motion pattern recognition algorithm was integrated with the ZUPT algorithm to achieve adaptive adjustment of the zero-speed determination thresholds for the pedestrian movement trajectories containing multiple motion patterns.

F. Attitude update

The Extended Kalman Filter (EKF) algorithm is commonly applied in attitude update calculations. In addition to EKF, there are other methods such as Unscented Kalman Filter and Particle Filter. Compared to these methods, EKF has a lower computational complexity, making it suitable for real-time systems, particularly in resource-constrained environments [43]. By using EKF, we are able to strike a balance between accuracy and computational efficiency, ensuring that the system can operate efficiently and reliably in real-time under limited resources.

The extended Kalman filter discrete-time state-space nonlinear model is given as:

$$\begin{cases} X_t = f(X_{t-1}) + W_{t-1} \\ Z_t = h(X_t) + V_t \end{cases} \tag{18}$$

Where: X_t is the state quantity at moment t, Z_t is the observation quantity at moment t, W_{t-1} and V_t are the process noise and observation noise, respectively.

The nonlinear expanded Kalman filter formula for the state is given by

$$\begin{cases} \hat{X}_{t/t-1} = f(\hat{X}_{t-1}) \\ P_{t/t-1} = \Phi_{t/t-1}P_{t-1}\Phi_{t/t-1}^T + Q_{t-1} \\ K_t = P_{t/t-1}H_t^T(H_tP_{t/t-1}H_t + R_t)^{-1} \\ \hat{X}_t = \hat{X}_{t/t-1} + K_t\left[Z_t - h(\hat{X}_{t/t-1})\right] \\ P_t = (I - K_tH_t)P_{t/t-1} \end{cases} \tag{19}$$

Where: $\hat{X}_{t-1}$ and $\hat{X}_t$ denote the a posteriori state estimates at time $t-1$ and t, respectively, $\hat{X}_{t/t-1}$ is the a priori state estimate at time t, $P_{t/t-1}$ and P_{t-1} are the a priori estimation error covariance array at time t and the a posteriori estimation error covariance array at moment $t-1$, respectively, $K_t$is the filter gain, P_t is the a posteriori estimate at time t, $\Phi_{t/t-1}$) is the state transfer matrix obtained by solving the Jacobian matrix for the state quantities by $f(\hat{X}_{t-1})$, H_t is the observation matrix obtained by solving the Jacobian matrix for the state quantities by $h(\hat{X}_{t/t-1})$, I is the unit matrix.

To correct the heading angle and offset in the forward direction effectively, relying solely on the ZUPT algorithm is insufficient. To enhance system robustness, the observation process was divided into two levels: the normalized values of the accelerometer and gyroscope measurements as the first observation, and the normalized values of the magnetometer measurements as the second observation.

To mitigate the impact of linear acceleration combined with gravitational acceleration on accelerometer data, an adaptive accelerometer observation noise covariance operator was introduced in the first-level filtering. Similarly, an adaptive magnetometer observation noise covariance operator was introduced in the second-level filtering to reduce the influence of external magnetic interference on magnetometer readings. Therefore, the updated Equation (20) is:

$$\begin{cases} \hat{X}_{t/t-1} = f(\hat{X}_{t-1}) \\ P_{t/t-1,1} = \Phi_{t/t-1}P_{t-1}\Phi_{t/t-1}^T + Q_{t-1} \\ K_{t,1} = P_{t/t-1,1}H_{t,1}^T(H_{t,1}P_{t/t-1,1}H_{t,1}^T + R_{t,1})^{-1} \\ \hat{X}_{t,1} = \hat{X}_{t/t-1} + K_{t,1}\left[Z_{t,1} - h_1(\hat{X}_{t/t-1})\right] \\ P_{t,1} = \left(I - K_{t,1}H_{t,1}\right)P_{t/t-1,1} \\ K_{t,2} = P_{t,1}H_{t,2}^T(H_{t,2}P_{t,1}H_{t,2}^T + R_{t,2})^{-1} \\ \hat{X}_t = \hat{X}_{t,1} + K_{t,2}\left[Z_{t,2} - h_2(\hat{X}_{t,1})\right] \\ P_t = (I - K_{t,2}H_{t,2})P_{t,1} \end{cases} \tag{20}$$

Where: $P_{t/t-1,1}$ and P_{t-1} are the a priori estimation error covariance array of the first-level filter at moment t and the a posteriori estimation error covariance array at moment $t-1$, respectively, $K_{t,1}$ is the filter gain in the first-stage filtering, $H_{t,1}$ is the observation matrix in the first-stage filtering, $R_{t,1}$ is the observation noise matrix in one level of filtering, $h_1(\hat{X}_{t/t-1})$ is the observation equation of the accelerometer, $H_{t,1}$ is the result of solving the Jacobi matrix for the state quantities by $h_1(\hat{X}_{t/t-1})$, $\hat{X}_{t,1}$ is the a posteriori estimate of the state in the first level of filtering at moment t, $P_{t,1}$ is the a posteriori estimate error covariance array of the first level of filtering at moment t, $K_{t,2}$ is the filter gain in the second-level filtering, $\hat{X}_t$ is the a posteriori estimate of the state in the secondary filter at moment t, $H_{t,2}$ is the observation matrix in the secondary filter, $R_{t,2}$ is the observation noise matrix in the secondary filter, $h_2(\hat{X}_{t,1})$ is the observation equation for the

magnetometer, $H_{t,2}$is the result of solving the Jacobi matrix for the state quantities by $h_2(\hat{X}_{t,1})$.

G. Data transmission scheme

A Body Area Network (BAN) was established for data transmission, employing a central micro-host and multi-motion measurement nodes architecture. The BAN includes an internal 2.4GHz network with a star topology, where the root node is a sensor placed at the lower back. Compared to chain and tree topologies, the star topology offers lower latency and better synchronization performance. However, it places higher demands on the central node in terms of computational load, bandwidth handling, and reliability [44].

To manage congestion and ensure efficient, real-time data transmission, an enhanced Transmission Control Protocol (TCP) Illinois algorithm was adopted. While more recent congestion control protocols such as BBR (Bottleneck Bandwidth and Round-trip propagation time) and QUIC (Quick UDP Internet Connections) have gained popularity in internet-scale applications, they are less suitable for embedded wearable systems [45], [46]. Specifically, BBR often exhibits bursty bandwidth behavior and higher CPU overhead, which challenges real-time scheduling on lightweight processors like the ESP32. QUIC, as a user-space protocol integrated with TLS and HTTP/3 stacks, introduces significant complexity and has limited microcontroller support. In contrast, TCP-Illinois offers a favorable trade-off between throughput and delay, with low implementation overhead, making it particularly suitable for resource-constrained real-time BAN environments [47].

To further improve TCP-Illinois performance under dynamic network conditions, we introduce a congestion differentiation strategy that distinguishes between random and congestion-induced packet loss. The method for differentiating packet loss types is based on estimating the backlog in the bottleneck queue, with the backlog quantity N calculated using the following formula:

$$\begin{cases} N = A * (Rtt - MinRtt) = \Delta V * MinRtt \\ \Delta V = \frac{Cw}{MinRtt} - \frac{Cw}{Rtt} \end{cases} \quad (21)$$

Where: A is the actual sending rate, Rtt is the round-trip delay value obtained from the last measurement, $MinRtt$ denotes the minimum Rtt value measured throughout the process, ΔV denotes the difference between the desired rate and the actual rate, and Cw denotes the size of the current congestion window.

To further enhance the estimation of bandwidth, this study monitors the Acknowledge character (ACK) response rate during the TCP handshake protocol, with the sampled data undergoing smoothing. The calculated backlog quantity N is then compared with a threshold value β (set to either 3 or 6) to distinguish the current type of packet loss. Based on the estimated bandwidth, the congestion window is adjusted to maximize the utilization of network bandwidth resources, thereby improving network throughput. This communication structure not only minimizes latency but also enhances system robustness against packet loss and transmission interference—both of which are critical for ensuring stable operation in dynamic environments. The star topology with an enhanced congestion control mechanism enables the system to support multiple sensor nodes while maintaining synchronization integrity, contributing to its robustness and scalability. The overall workflow of the BAN is illustrated in Figure 6.

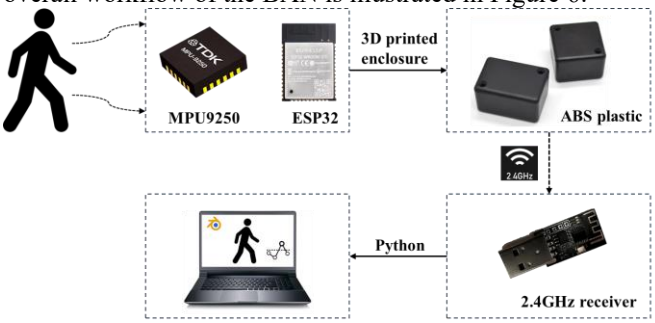

Fig. 6 Components of the Body Area Network.

H. Construction and driving of digital twin models

In this work, a 13-node digital twin model of the human body was developed based on human kinematic modeling. The human body is segmented into upper and lower limbs with the hip as the central boundary. During motion, proximal skeletal segments initiate movement to overcome inertia, leading to sequential motion across interconnected joints and limbs [48].

The lumbar spine node is designated as the root bone of the digital twin model, anchoring the torso and limbs. Real-time visualization is implemented using Blender, a widely adopted 3D animation software. Python scripts executed in Blender retrieve and decode serial port data, store it in a global joint data dictionary, and bind joint angles to the virtual skeleton via multithreaded execution. To ensure consistent temporal alignment between data streams, each joint's motion update is handled asynchronously, and packet delays or losses are discarded to avoid desynchronization.

Sensor data is streamed at approximately 60 Hz using the pyserial library, while the network transmission latency—measured at 13.17 ms—is sufficient to support real-time rendering rates above 60 Hz. This allows smooth integration with Blender's frame rate (typically 30–60 FPS), ensuring near-instantaneous mirroring of physical motion in the digital model.

To support high-fidelity rendering under real-time constraints, the 3D avatar was optimized with mesh simplification (average polygon count < 10,000) and GPU-based skinning. The system was tested on a machine equipped with an Intel i7 processor and NVIDIA RTX 2060 GPU, achieving an average rendering performance of 45 frames per second during multi-joint movement.

Beyond passive motion mapping, the digital twin model serves as an interactive and responsive avatar. It enables bi-directional communication: real-world movements are mirrored in real time, while the virtual environment can provide visual cues, posture corrections, or task-specific prompts. This closed-loop feedback system enhances user engagement, situational awareness, and system responsiveness in applications such as physical rehabilitation, sports coaching, and immersive virtual scenarios, as shown in Figure 7.

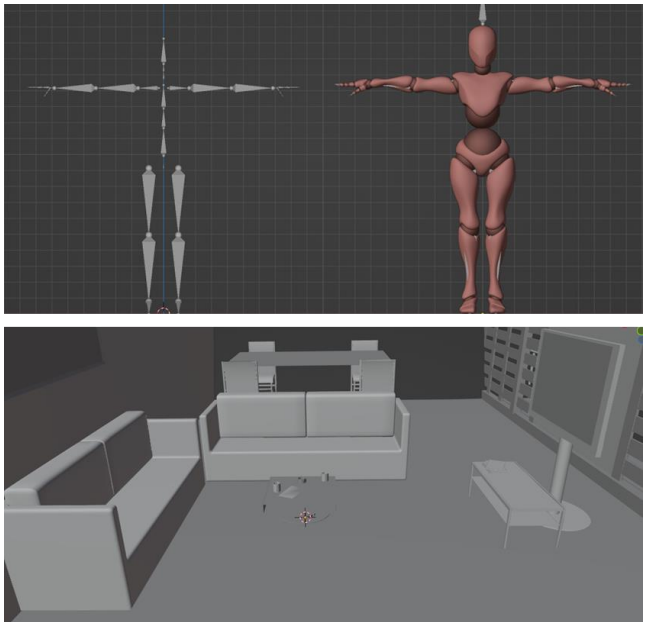

Fig. 7 Construction and schematic diagram of the digital twin model.

IV. Experimental Validation

To validate the performance of the proposed smart bodysuit system in human motion state monitoring, this section provides a detailed evaluation of the system focusing on accuracy, robustness, and user experience.

A. Network latency testing

The experiment aimed to measure the network latency (the delay in the transmission of data from the sensors to the PC) of the system using the enhanced TCP-Illinois congestion control algorithm compared to the system without it, focusing on the time required for the Root node to complete polling all sensor nodes after they updated their data. The experimental setup was as follows: the sensor nodes were configured to immediately respond with 8 bytes of data upon receiving a command from the Root node. A high-precision timer was set up on the Root node, starting when the Root node sent the first polling command and stopping immediately after receiving the response from the 100th polling cycle, recording the total latency time. To ensure accuracy, the experiment was conducted in a relatively isolated and stable network environment to avoid external interference. The experiment was repeated 10 times to calculate the average latency and standard deviation. The test results, shown in Figure 8, indicate that the average network latency of the sensor data transmission to the PC was 13.17 ms with the algorithm (Group A), compared to 57.21 milliseconds without it (Group B).

For comparison, the Noitom Perception Neuron 3 system reports a latency of 30 milliseconds [28], while the Rokoko Smartsuit Pro II claims a latency of approximately 15 milliseconds, depending on the Wi-Fi router used [49]. Therefore, the system proposed in this work demonstrates latency performance that is comparable to, or even better than, commercial systems.

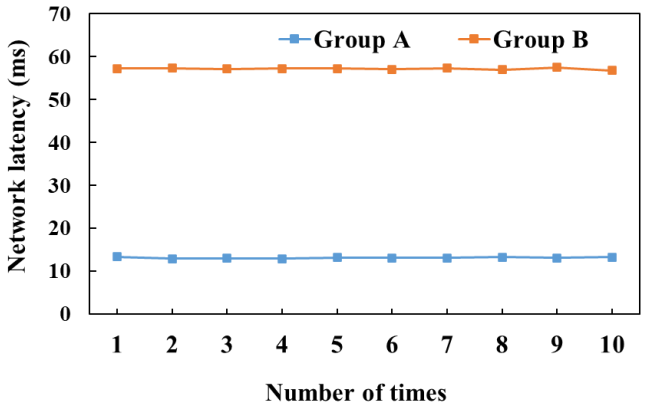

Fig. 8 Network latency test results.

TABLE I
RESULTS OF JOINT ANGLE ACCURACY TESTING

Actual angle (°)		30	60	90	120	150
Absolute value of error (°)	1	0.09	0.08	0.16	0.13	0.05
	2	0.14	0.11	0.18	0.15	0.09
	3	0.24	0.31	0.27	0.19	0.16
	4	0.07	0.15	0.17	0.22	0.12
	5	0.26	0.1	0.07	0.27	0.06
	6	0.11	0.24	0.22	0.17	0.14
RMSE		0.17	0.18	0.19	0.19	0.11

Note: RESM denotes root mean square error

B. Joint angle accuracy testing

According to Equations 1-4, it can be seen that the rotation angle of the joints is a key variable in the process of kinetic model derivation, so whether the joint angle can be calculated accurately is a key evaluation index of the motion capture system.

To verify the consistency between the joint angles calculated by the sensors and the actual joint angles, a mechanical arm suitable for angle analysis was assembled. In the experiment, two sensors used for measuring joint angles were fixed on the support arms of the mechanical arm, and the rotational speed and angle of the motors were controlled by the No.1 and No.2 channels (high-speed channels) of the ESP32 microcontroller, respectively, with the frequency of the PWM wave set to 90Hz and the accuracy of the motors set to 0.05°.

During the test, the mechanical arm was initially set at 30° and held stationary for 20 seconds. Subsequently, it was rotated by 30° increments and again held for 20 seconds, gradually reaching up to 150°, with these steps repeated across six experiments.

The statistics for the six experiments are shown in Table 1, and Figure 9 shows the results for one of the experiments, demonstrate that the absolute error in joint angle measurement was controlled within 0.2°. This data demonstrates that the

system's joint angle measurement accuracy is comparable to or even better than traditional motion capture devices [48], proving that the proposed system meets the requirements for measuring joint angles in motion.

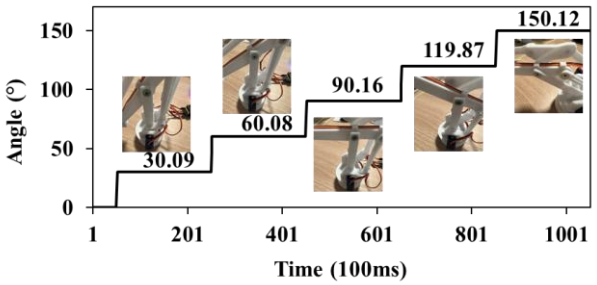

Fig.9 Mechanical arm used to measure joint angles and the test results.

C. Recognition test of motion patterns

In order to test the recognition effect of the RF algorithm proposed in this work on different motion states, the proposed motion state classification model was validated using the 7-fold cross-validation method.

The method for selecting the test set and the results of motion mode recognition are illustrated in Figure 10. Through testing, the motion state classification model proposed in this work demonstrated excellent recognition performance for the five motion states, with recognition rates reaching up to 99%.

To provide a more rigorous statistical evaluation of our motion recognition model, we report additional metrics including precision, recall, and F1-score in addition to accuracy. The results are based on 7-fold cross-validation across five motion classes (standing, walking, running, ascending stairs, descending stairs, sitting, jumping, and squatting). Table II summarizes the averaged results across folds. Despite the increase in complexity, the model achieved an overall recognition accuracy of 98.6%.

To further evaluate the generalizability of the proposed model, we conducted a cross-dataset validation by training the classifier using the DIP-IMU dataset and testing it on the TotalCapture dataset. Despite differences in sensor placement and subject variability between datasets, our model achieved an overall classification accuracy of 96.4%, suggesting strong cross-domain generalization capability. The result demonstrates that the adaptive threshold method maintains robustness across diverse data sources and motion capture environments.

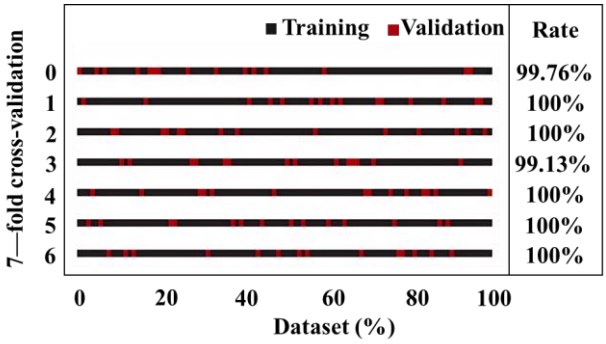

Fig.10 Seven-fold cross-validation method and the recognition rate.

TABLE II
RESULTS OF RECOGNITION ACCURACY TESTING

Motion Class	Precision (%)	Recall (%)	F1-Score (%)
Standing	98.6	99.1	98.8
Walking	99.3	99.0	99.1
Running	98.8	98.5	98.6
Ascending Stairs	98.9	98.7	98.8
Descending Stairs	99.0	98.6	98.8
Jumping	98.9	98.7	98.3
Sitting	97.7	98.3	97.1
Squatting	97.3	97.5	97.4
Average	98.6	98.5	98.4

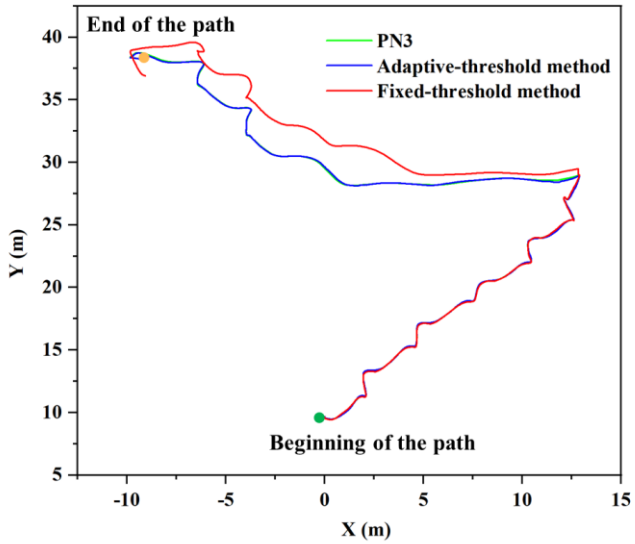

Fig. 11 Planar displacement calculation results of the two methods.

D. Orientation accuracy testing

To assess the effectiveness of the adaptive-threshold method proposed in this work compared to traditional fixed-threshold methods, a comparison of data accuracy between the two methods was conducted. During the experiment, participants wore the smart bodysuit system, and the Notiom Perception Neuron 3 (Notiom Ltd., China) were strapped at the position of the IMU on the right calf. The data collected from the Notiom Perception Neuron 3 served as the gold standard, with the participants repeating the same walking trajectory in two separate experiments.

Figure 11 displays the results of planar positioning using both fixed-threshold (Group A) and adaptive-threshold methods (Group B) with the IMU located on the calf during participant movement, contrasted against data collected by Notiom Perception Neuron 3. Based on the results, in the initial stages of motion, due to the smaller cumulative error of the sensor, the planar data tested by both methods were

relatively close. However, after walking a certain distance, the cumulative error with the fixed-threshold method becomes more significant, resulting in noticeable drift in planar positioning, with a average relative position error of 4.26%. Conversely, the planar positioning results from the adaptive-threshold method closely align with the data collected by Notiom Perception Neuron 3, with an average relative position error of 0.33%. This indicates that the system's positioning accuracy is significantly improved by adopting the proposed adaptive threshold method.

To further clarify the practical advantage of the proposed RF+ZUPT-based adaptive-threshold method, we conducted a comparative evaluation against typical deep learning-based motion classification models, including LSTM [51], 1D CNN [52], and TinyML [53]. All models were trained and tested on the same dataset comprising five common movement patterns (standing, walking, running, ascending stairs, descending stairs). The deep models were implemented using TensorFlow Lite and benchmarked on an ESP32-based edge computing platform. As shown in Table III, while deep learning models achieve comparable classification accuracy (96.6–97.3%), they incur significantly higher computational cost, model size, and inference latency. Notably, the LSTM model requires more than 1.2MB of memory and an average inference time of 29.5ms per frame, which exceeds the processing capacity of our embedded system. In contrast, our proposed method achieves 98.6% accuracy with only 3.2ms latency and 480KB model size, demonstrating superior suitability for real-time wearable applications.

In summary, our proposed method provides a balanced trade-off between accuracy, computational efficiency, and deployment feasibility, making it highly suitable for smart textile systems and embedded digital twin applications.

TABLE III
RESULTS OF RECOGNITION ACCURACY TESTING

Motion Class	Accuracy (%)	Model Size (KB)	Inference Latency (ms/frame)
LSTM	96.6	1210	29.5
1D CNN	97.3	930	23.7
TinyML	96.8	360	8.9
RF+ZUPT	**98.6**	**480**	**3.2**

E. Motion trajectory testing

Following the validation of the system accuracy in recognizing motion states and joint angles, this study further evaluated the effectiveness of the proposed smart bodysuit system in practical motion tests, including real-time posture and position tracking.

An experimental laboratory with classic indoor features such as long-distance channels and staircases was selected as the testing site. The test was performed by a participant wearing the smart bodysuit system proposed in this study and following the guidance. The testing process included walking, running, jumping, climbing stairs, and sitting stages, with simultaneous collection of sensor data from the proposed smart bodysuit system.

Figure 12 illustrates the entire experimental process and the trajectory of skeletal movements during the testing process. The experimental results demonstrate that this smart bodysuit system can achieve real-time tracking of human posture.

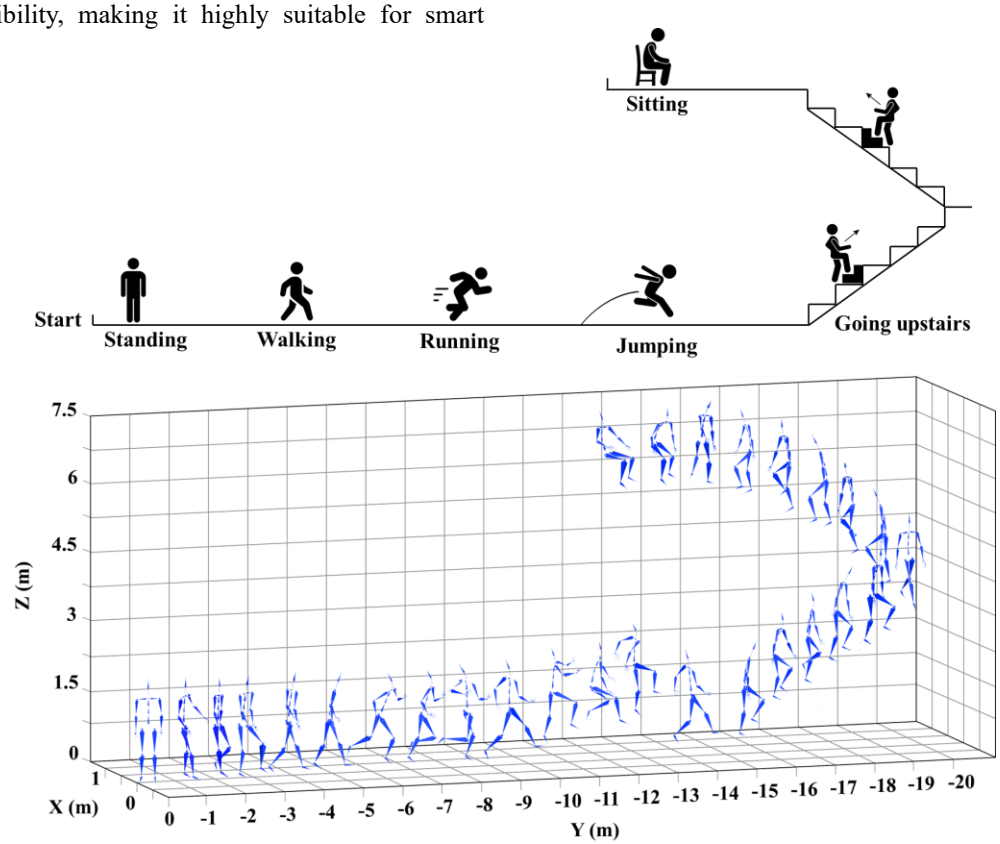

Fig. 12 The flow of motion trajectory testing and motion test results of the whole body.

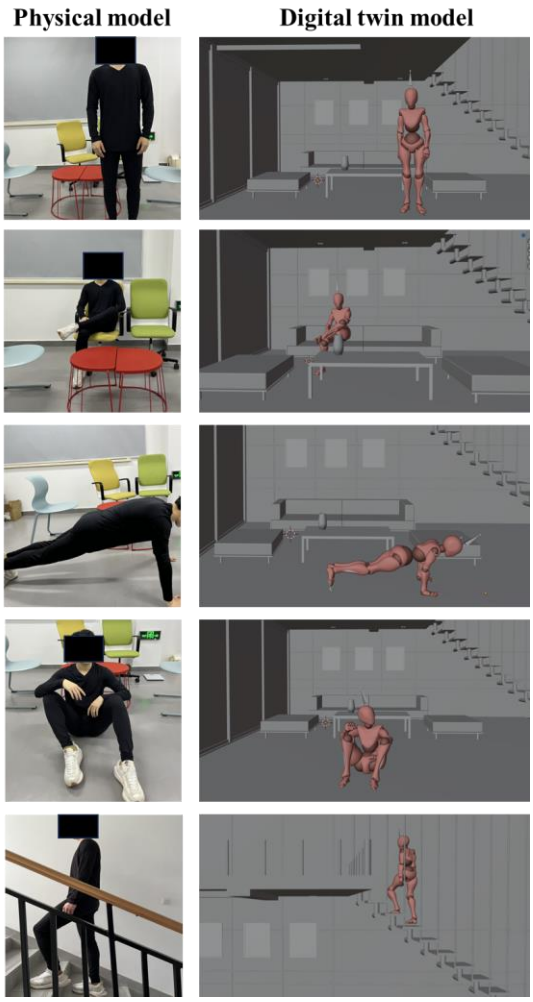

Fig. 13 Linkage test diagram of physical model and digital twin model of smart bodysuit system.

F. Stress Testing for digital twin model

To preliminarily evaluate the system's scalability and robustness, we conducted stress tests by gradually increasing the number of active sensor nodes from 5 to 15 while monitoring latency and synchronization deviation. Based on the human node model established in section 3, the digital twin model of the smart bodysuit system and the digital twin model of the real scenario were imported into Blender software. Real-time data streams were transmitted to the model using Python. The results showed that the average network latency remained below 20 ms, and no packet loss occurred, validating the system's scalability.

Further tests were conducted to assess robustness under dynamic and potentially disruptive conditions. These included high-mobility tasks (e.g., running, stair climbing) and scenarios with significant wireless interference (e.g., operating near multiple active Wi-Fi sources).

In all cases, the system maintained data integrity, stable synchronization, and consistent visualization, confirming its robustness in complex real-world environments. Figure 13 shows the synchronous relationship between the digital twin model in Blender and the physical "clothing-human-environment" system during testing. The test demonstrates that the real state of the user and the environment can be restored by the digital twin model of the system, enabling interaction within the "clothing-human-environment" scenario.

G. User experience testing

To compare user experience differences between clothing-based carriers and strap-based carriers, a subjective evaluation experiment was designed. The experimental objects included commercially available straps (control group, Group A) and the smart bodysuit proposed in this work (Group B), as shown in Figure 14(a). Evaluation criteria included aesthetics, wearability, heaviness, restrictiveness movement, and overall comfort, the Fritz five-level semantic differential scale was used for scoring, as shown in Table 1.

Twelve participants (height: 173.6 ± 4.9 cm, weight: 65.3 ± 7.6 kg) were invited to participate in the user experience testing conducted in a laboratory with a temperature of 25(±1)°C, humidity of 50(±3)%, and wind speed less than 0.1 m/s. The test was divided into four stages.

1) Wearing stage: participants were asked to wear clothing or straps on their own, and the time taken was recorded by staff.

2) Sitting stage: Participants remained seated for 2 minutes.

3) Prescribed activity Stage: Participants performed designated activities such as walking slowly, squatting, and going up and down stairs for 2 minutes.

4) Free activity stage: Participants engaged in free activities based on personal preference for 2 minutes.

Subjective evaluation scores were provided by participants at the end of each stage, and all experimental conditions, procedures, and participants were consistent across both experiments.

The evaluation scores for the two experimental objects by participants are depicted in Figure 14(b). The results indicated that the average scores for aesthetics, wearability, heaviness, restrictiveness movement, and overall comfort were higher for Group B (smart bodysuit) compared to Group A (strap) by 91.6%, 150%, 71.7%, 70.6%, and 149.6%, respectively, resulting in an overall score 99.1% higher for Group B.

Additionally, participants spent significantly less time donning the experimental object in Group B (28.3 seconds) compared to Group A (270.3 seconds). This experiment demonstrates that the proposed smart bodysuit system in this work is far superior to traditional strap-based wearable devices in terms of comfort, usability, and user experience.

To further quantify the ergonomic performance of the smart bodysuit, especially its thermal comfort under long-term wear, we additionally evaluated the thermal and evaporative resistance of the bodysuit using a thermal manikin, as shown in Figure 14(c). The test was conducted in accordance with ISO 15831:2004 standard procedures [54]. Measurements were performed under controlled conditions (ambient temperature: 20 ± 1°C, relative humidity: 65 ± 5%, air velocity: < 0.1 m/s). Two configurations were assessed: (1) the base bodysuit without hardware modules, and (2) the bodysuit with fully installed sensor and controller components. The difference in

thermal resistance and evaporative resistance between the two configurations reflects the impact of embedded hardware on the overall thermal comfort. Results indicated a minimal increase in thermal resistance and evaporative resistance (by 1.3% and 1.5% respectively), suggesting that the modular design and placement of the hardware components do not significantly impair the bodysuit's breathability and heat dissipation. These findings support the suitability of the smart bodysuit for extended use in daily scenarios.

TABLE I
FRITZ FIVE-LEVEL SEMANTIC DIFFERENTIAL SCALE

Adjective (negative)	1	2	3	4	5	Adjective (positive)
	Extremely	Quite	Moderate	Quite	Extremely	
Ugly	◄				►	**Beautiful**
Inconvenient	◄				►	**Convenient**
Heavy	◄				►	**Light**
Restricted	◄				►	**Relaxed**
Uncomfortable	◄				►	**Comfortable**

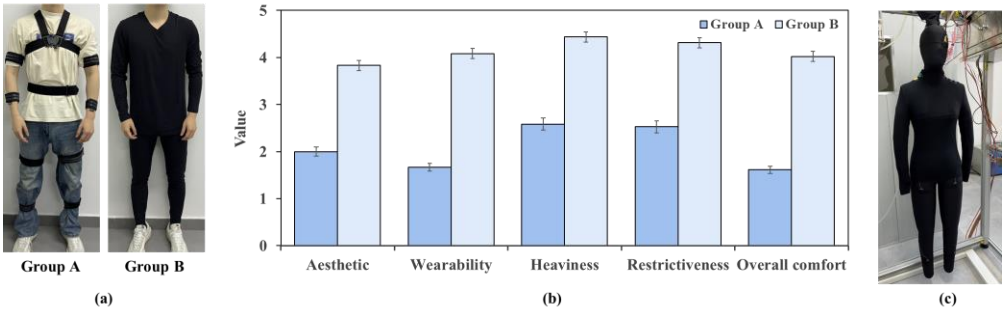

Fig. 14 (a) Wearing effect of test subjects; (b) Test results; (c) Measurement of thermal and moisture resistance of bodysuit using a heated sweating manikin.

V. Discussion

In this work, a smart bodysuit system incorporating digital twin technology for real-time human motion monitoring and visualization was proposed to cope with the shortcomings of existing motion monitoring or capturing devices in terms of accuracy, usability, comfort and interactivity.

The smart bodysuit system consists of two components: the physical system and the virtual system. The physical system includes the garment and hardware modules designed to collect and transmit human motion data, while the virtual system comprises 3D modeling software and digital twin models for receiving and displaying motion data. To enhance comfort, aesthetics, and wearability, a knitted bodysuit was designed to house the hardware modules, which were optimized for size, weight, and power consumption. To reduce calibration errors, a calibration method was introduced that accounts for misalignment between the garment and the skeleton. Additionally, a novel multi-mode motion adaptive threshold method, combining RF algorithms and ZUPT algorithms, was implemented to improve zero-velocity detection performance. An enhanced TCP-Illinois congestion control algorithm was also proposed to reduce system latency. Furthermore, digital twin technology was integrated into the smart bodysuit system to enhance human-computer interaction.

A series of tests conducted on the system demonstrated low latency, high accuracy, and good comfort and wearability. The network latency test showed a delay of 13.17 milliseconds, which is comparable to or even better than commercial systems. Joint angle tests indicated that the system's measurement error was less than 0.2°. The motion pattern recognition method, based on the RF algorithm, achieved an accuracy rate of 98.6%. The proposed adaptive threshold calculation method outperformed the fixed threshold method in terms of accuracy. Subjective user testing demonstrated significant improvements in comfort, aesthetics, and ease of use compared to conventional strap-based systems. In particular, donning time was reduced by nearly 90%. To further assess long-term wearability, we evaluated the thermal comfort of the bodysuit using a thermal manikin. Testing revealed only minor increases in thermal and evaporative resistance after hardware integration, confirming that the design maintains good breathability and is suitable for extended use. Additionally, 3D software

integration tests revealed that the smart bodysuit system not only captures the wearer's motion data but also reconstructs real user activity states through digital twin models. These features make the system suitable for applications in metaverse environments, digital healthcare, home monitoring, and sports science.

These features make the system not only a motion monitoring device but also a responsive interactive platform, suitable for applications in metaverse environments, digital healthcare, home monitoring, and sports science. Looking forward, we envision further improvements through the integration of smart textiles (e.g. self-powered textile, flexible sensors and lightweight on-body computing). These enhancements would elevate the smart bodysuit system into a fully autonomous, textile-native digital twin platform, pushing the boundary of wearable intelligence and immersive motion representation. In parallel, we also plan to address long-term sensor drift through extended-duration testing and integration of periodic recalibration or multi-sensor fusion techniques, to further enhance the system's stability in diverse and unconstrained scenarios.

ACKNOWLEDGMENT

The authors wish to acknowledge the volunteers for their assistance in this work

REFERENCES

[1] O. M. Giggins, K. T. Sweeney, and B. Caulfield, "Rehabilitation exercise assessment using inertial sensors: a cross-sectional analytical study," *J. Neuroeng. Rehabil*., vol. 11, no. 1, pp. 1-10, Jan. 2014, doi: 10.1186/1743-0003-11-1.

[2] Y. Wang, Y. Han, and Q. Wang, "The application of motion trajectory acquisition and intelligent analysis technology in physical education teaching in colleges and universities," *Secur. Commun. Netw*., vol. 2022, no. 1, pp. 1-13, Jan. 2022, doi: 10.1155/2022/9193741.

[3] Y. Song, D. Demirdjian, and R. Davis, "Continuous body and hand gesture recognition for natural human-computer interaction," *ACM Trans. Interact. Intell. Syst.*, vol. 2, no. 1, pp. 1-28, Mar. 2012, doi: 10.1145/2133366.2133371.

[4] M. Simonetto, S. Arena, and M. Peron, "A methodological framework to integrate motion capture system and virtual reality for assembly system 4.0 workplace design," *Saf. Sci.*, vol. 146, Art. no. 105561, Sep. 2022, doi: 10.1016/j.ssci.2021.105561.

[5] C. Bregler, "Motion capture technology for entertainment," *IEEE Signal Process. Mag*., vol. 24, no. 6, pp. 160-158, Nov. 2007, doi: 10.1109/MSP.2007.905896.

[6] L. Žlajpah and T. Petrič, "Kinematic calibration for collaborative robots on a mobile platform using motion capture system," *Robot. Comput.-Integr. Manuf*., vol. 79, Art. no. 102446, Feb. 2023, doi: 10.1016/j.rcim.2022.102446.

[7] Y. Wang, L. Wang, T. Yang, et al., "Wearable and highly sensitive graphene strain sensors for human motion monitoring," *Adv. Funct. Mater.*, vol. 24, no. 29, pp. 4666-4670, Aug. 2014, doi: 10.1002/adfm.201400221.

[8] S. Z. Homayounfar and T. L. Andrew, "Wearable sensors for monitoring human motion: a review on mechanisms, materials, and challenges," *SLAS Technol*., vol. 25, no. 1, pp. 9-24, Feb. 2020, doi: 10.1177/2472630319880958.

[9] C. C. Yang and Y. L. Hsu, "A review of accelerometry-based wearable motion detectors for physical activity monitoring," *Sensors*, vol. 10, no. 8, pp. 7772-7788, Aug. 2010, doi: 10.3390/s100807772.

[10] B. Peng, F. Zhao, J. Ping, et al., "Recent advances in nanomaterial‐enabled wearable sensors: material synthesis, sensor design, and personal health monitoring," *Small*, vol. 16, no. 44, Art. no. 2002681, Nov. 2020, doi: 10.1002/smll.202002681.

[11] C. Auepanwiriyakul, S. Waibel, J. Songa, et al., "Accuracy and acceptability of wearable motion tracking for inpatient monitoring using smartwatches," *Sensors*, vol. 20, no. 24, Art. no. 7313, Dec. 2020, doi: 10.3390/s20247313.

[12] G. Cosoli, S. Spinsante, and L. Scalise, "Wrist-worn and chest-strap wearable devices: Systematic review on accuracy and metrological characteristics," *Meas*., vol. 159, Art. no. 107789, Dec. 2020, doi: 10.1016/j.measurement.2020.107789.

[13] M. Giurgiu, S. Ketelhut, C. Kubica, et al., "Assessment of 24-hour physical behaviour in adults via wearables: a systematic review of validation studies under laboratory conditions," *Int. J. Behav. Nutr. Phys. Act*., vol. 20, no. 1, Art. no. 68, Jun. 2023, doi: 10.1186/s12966-023-01456-7.

[14] U. G. Longo, S. De Salvatore, A. Carnevale, et al., "Optical motion capture systems for 3D kinematic analysis in patients with shoulder disorders," *Int. J. Environ. Res. Public Health,* vol. 19, no. 19, Art. no. 12033, Sep. 2022, doi: 10.3390/ijerph191912033.

[15] A. Dasgupta, R. Sharma, C. Mishra, et al., "Machine Learning for Optical Motion Capture-Driven Musculoskeletal Modelling from Inertial Motion Capture Data," *Bioengineering*, vol. 10, no. 5, Art. no. 510, May 2023, doi: 10.3390/bioengineering10050510.

[16] K. Chen, Y. Wang, S. H. Zhang, et al., "Mocap-solver: A neural solver for optical motion capture data," *ACM Trans. Graph.*, vol. 40, no. 4, pp. 1-11, Aug. 2021, doi: 10.1145/3450626.3459823.

[17] H. Hu, Z. Cao, X. Yang, et al., "Performance evaluation of optical motion capture sensors for assembly motion capturing," *IEEE Access*, vol. 9, pp. 61444-61454, Apr. 2021, doi: 10.1109/ACCESS.2021.3073998.

[18] S. E. Kessler, M. J. Rainbow, G. A. Lichtwark, et al., "A direct comparison of biplanar videoradiography and optical motion capture for foot and ankle kinematics," *Front. Bioeng. Biotechnol*., vol. 7, Art. no. 199, Jul. 2019, doi: 10.3389/fbioe.2019.00199.

[19] A. Szczęsna, M. Błaszczyszyn, and M. Pawlyta, "Optical motion capture dataset of selected techniques in beginner and advanced Kyokushin karate athletes," *Sci. Data*, vol. 8, no. 1, Art. no. 13, Jan. 2021, doi: 10.1038/s41597-021-00829-w.

[20] M. Bortolini, M. Gamberi, F. Pilati, et al., "Automatic assessment of the ergonomic risk for manual manufacturing and assembly activities through optical motion capture technology," *Procedia CIRP,* vol. 72, pp. 81-86, Aug. 2018, doi: 10.1016/j.procir.2018.03.189.

[21] V. Ricotti, B. Kadirvelu, V. Selby, et al., "Wearable full-body motion tracking of activities of daily living predicts disease trajectory in Duchenne muscular dystrophy," *Nat. Med*., vol. 29, no. 1, pp. 95-103, Jan. 2023, doi: 10.1038/s41591-022-02034-4.

[22] D. Vlasic, R. Adelsberger, G. Vannucci, et al., "Practical motion capture in everyday surroundings," *ACM Trans. Graph*., vol. 26, no. 3, Art. no. 35, Aug. 2007, doi: 10.1145/1276377.1276437.

[23] R. V. Vitali and N. C. Perkins, "Determining anatomical frames via inertial motion capture: A survey of methods," *J. Biomech.*, vol. 106, Art. no. 109832, Jul. 2020, doi: 10.1016/j.jbiomech.2020.109832.

[24] J. Li, X. Liu, Z. Wang, et al., "Real-time human motion capture based on wearable inertial sensor networks," *IEEE Internet Things J*., vol. 9, no. 11, pp. 8953-8966, Jun. 2021, doi: 10.1109/JIOT.2021.3064479.

[25] S. Qiu, H. Zhao, N. Jiang, et al., "Sensor network oriented human motion capture via wearable intelligent system," *Int. J. Intell. Syst.*, vol. 37, no. 2, pp. 1646-1673, Feb. 2022, doi: 10.1002/int.22651.

[26] Q. Liu, "Human motion state recognition based on MEMS sensors and Zigbee network," *Comput. Commun.*, vol. 181, pp. 164-172, May 2022, doi: 10.1016/j.comcom.2022.02.008.

[27] Xsens, "Motion Capture, 3D Motion Tracking System," https://www.xsens.com, Accessed: Aug. 11, 2024.

[28] Noitom, "Noitom - Motion Capture Technology," https://www.noitom.com.cn/, Accessed: Aug. 11, 2024.

[29] C. Liu, R. Gu, J. Yang, et al., "A self-powered dual ratchet angle sensing system for digital twins and smart healthcare," *Adv. Funct. Mater.*, vol. 34, no. 42, Art. no. 2405104, 2024.

[30] Y. Xiong, Z. Huo, J. Zhang, et al., "Triboelectric in-sensor deep learning for self-powered gesture recognition toward

multifunctional rescue tasks," *Nano Energy*, vol. 124, Art. no. 109465, 2024.

[31] M. Jamshidi, D. T. Hoang, and D. N. Nguyen, "CNN-FL for biotechnology industry empowered by Internet-of-BioNano Things and digital twins," *IEEE Internet Things Mag.*, vol. 7, no. 5, pp. 54–63, 2024.

[32] P. Jin, R. T. Jiang, and L. Shen, "Development and evaluation of a multi-functional welding protective clothing system," *J. Ind. Text.*, vol. 53, Art. no. 15280837231201380, 2023.

[33] P. Jin, R. Jiang, Q. Chen, et al., "Design and evaluation of multifunctional protective clothing for tunnel workers,"*Int. J. Occup. Saf. Ergon.*, vol. 29, no. 2, pp. 484–493, 2023.

[34] M. B. Jamshidi, S. Sargolzaei, S. Foorginezhad, et al., "Metaverse and microorganism digital twins: A deep transfer learning approach," *Appl. Soft Comput*., vol. 147, Art. no. 110798, 2023.S.

[35] H. Eryuruk and F. Kalaoglu, "Analysis of the performance properties of knitted fabrics containing elastane," *Int. J. Cloth. Sci. Technol*., vol. 28, no. 4, pp. 463-479, Jun. 2016, doi: 10.1108/IJCST-02-2016-0013.

[36] S. Y. Aleshinsky and V. M. Zatsiorsky, "Human locomotion in space analyzed biomechanically through a multi-link chain model," *J. Biomech.*, vol. 11, no. 3, pp. 101-108, Jun. 1978, doi: 10.1016/0021-9290(78)90021-4.

[37] T. Ishigaki and K. Yamamoto, "Dynamics computation of a hybrid multi-link humanoid robot integrating rigid and soft bodies," in Proc. 2021 IEEE/RSJ Int. Conf. Intell. Robots Syst. (IROS), Prague, Czech Republic,

[38] M. K. Kim, J. H. Choi, M. A. Gim, et al., "Effects of different types of exercise on muscle activity and balance control," *J. Phys. Ther. Sci*., vol. 27, no. 6, pp. 1875-1881, Jun. 2015, doi: 10.1589/jpts.27.1875.

[39] M. J. Duncan, Y. Al-Nakeeb, and J. Scurr, "Perceived exertion is related to muscle activity during leg extension exercise," *Res. Sports Med*., vol. 14, no. 3, pp. 179-189, Jul.-Sep. 2006, doi: 10.1080/15438620600854677.

[40] X. Zhang, C. Zhou, F. Chao, et al., "Low-cost inertial measurement unit calibration with nonlinear scale factors," *IEEE Trans. Ind. Inform.*, vol. 18, no. 2, pp. 1028-1038, Feb. 2021, doi: 10.1109/TII.2021.3074895.

[41] Y. Huang, M. Kaufmann, E. Aksan, et al., "Deep inertial poser: Learning to reconstruct human pose from sparse inertial measurements in real time," *ACM Trans. Graph.*, vol. 37, no. 6, Art. no. 185, Nov. 2018, doi: 10.1145/3272127.3275114.

[42] M. Trumble, A. Gilbert, C. Malleson, et al., "Total capture: 3D human pose estimation fusing video and inertial sensors," in Proc. 28th Brit. Mach. Vision Conf. (BMVC), London, U.K., 2017, pp. 1-13.

[43] J. H. Lee and N. L. Ricker, "Extended Kalman filter based nonlinear model predictive control," *Ind. Eng. Chem. Res*., vol. 33, no. 6, pp. 1530-1541, Jun. 1994, doi: 10.1021/ie00030a019.

[44] M. Barranco, J. Proenza, G. Rodríguez-Navas, et al., "An active star topology for improving fault confinement in CAN networks," *IEEE Trans. Ind. Inform*., vol. 2, no. 2, pp. 78-85, May 2006, doi: 10.1109/TII.2006.873999.

[45] N. Cardwell, et al., "BBR: Congestion-based congestion control," *Commun. ACM*, vol. 60, no. 2, pp. 58–66, Feb. 2017.

[46] Y. Cui, T. Li, C. Liu, X. Wang, and M. Kühlewind, "Innovating transport with QUIC: Design approaches and research challenges," *IEEE Internet Comput.*, vol. 21, no. 2, pp. 72–76, Mar./Apr. 2017.

[47] S. Abbasloo, C. Y. Yen, and H. J. Chao, "Wanna make your TCP scheme great for cellular networks? Let machines do it for you!," *IEEE J. Sel. Areas Commun.*, vol. 39, no. 1, pp. 265-279, Jan. 2020, doi: 10.1109/JSAC.2020.3018821.

[48] T. Fuse and K. Kamiya, "Statistical anomaly detection in human dynamics monitoring using a hierarchical Dirichlet process hidden Markov model," *IEEE Trans. Intell. Transp. Syst*., vol. 18, no. 11, pp. 3083-3092, Nov. 2017, doi: 10.1109/TITS.2017.2685630.

[49] Rokoko, "Motion Capture and Animation Tools," https://www.rokoko.com/, Accessed: Aug. 11, 2024.

[50] A. Ancans, M. Greitans, R. Cacurs, et al., "Wearable sensor clothing for body movement measurement during physical activities in healthcare," *Sensors*, vol. 21, no. 6, Art. no. 2068, Mar. 2021, doi: 10.3390/s21062068.

[51] L. Tong, R. Liu, and L. Peng, "LSTM-based lower limbs motion reconstruction using low-dimensional input of inertial motion capture system," *IEEE Sensors J.*, vol. 20, no. 7, pp. 3667–3677, Apr. 2020.

[52] E. Koşar and B. Barshan, "A new CNN-LSTM architecture for activity recognition employing wearable motion sensor data: Enabling diverse feature extraction," *Eng. Appl. Artif. Intell.*, vol. 124, Art. no. 106529, 2023.

[53] S. Gupta, S. Jain, B. Roy, et al., "A TinyML approach to human activity recognition," in *Proc. J. Phys.: Conf. Ser*., vol. 2273, no. 1, Art. no. 012025, 2022.

[54] E. N. ISO 15831, *Clothing—Physiological effects—Measurement of thermal insulation by means of a thermal manikin*, Brussels, Belgium: European Committee for Standardization, 2004.